Optical properties of highly nonlinear silicon-organic hybrid (SOH) waveguide geometries

Thomas Vallaitis,[1,*] Siegwart Bogatscher,[1] Luca Alloatti,[1] Pieter Dumon,[2]
Roel Baets,[2] Michelle L. Scimeca,[3] Ivan Biaggio,[3] François Diederich,[4]
Christian Koos,[1,5] Wolfgang Freude,[1] and Juerg Leuthold[1]

[1] Institute of Photonics and Quantum Electronics, University of Karlsruhe, 76131 Karlsruhe, Germany
[2] Photonics Research Group, Ghent University-IMEC, Dept. of Information Technology, B-9000 Gent, Belgium
[3] Department of Physics, Lehigh University, Bethlehem, PA 18015. USA
[4] Laboratorium für Organische Chemie, ETH Zürich, Hönggerberg, HCI, CH-8093 Zurich, Switzerland
[5] Now with Carl Zeiss AG, Corporate Research and Technology, 73447 Oberkochen, Germany
*t.vallaitis@ipq.uni-karlsruhe.de

Abstract: Geometry, nonlinearity, dispersion and two-photon absorption figure of merit of three basic silicon-organic hybrid waveguide designs are compared. Four-wave mixing and heterodyne pump-probe measurements show that all designs achieve high nonlinearities. The fundamental limitation of two-photon absorption in silicon is overcome using silicon-organic hybrid integration, with a five-fold improvement for the figure of merit (FOM). The value of FOM = 2.19 measured for silicon-compatible nonlinear slot waveguides is the highest value published.

OCIS codes: (190.3270) Kerr effect; (190.4360) Nonlinear optics, devices; (230.3120) Integrated optics devices; (230.4320) Nonlinear optical devices; (230.7370) Waveguides.

References and links

1. R. Salem, M. A. Foster, A. C. Turner, D. F. Geraghty, M. Lipson, and A. L. Gaeta, "Signal regeneration using low-power four-wave mixing on silicon chip," Nat. Photonics **2**(1), 35–38 (2007).
2. V. Mizrahi, K. W. DeLong, G. I. Stegeman, M. A. Saifi, and M. J. Andrejco, "Two-photon absorption as a limitation to all-optical switching," Opt. Lett. **14**(20), 1140–1142 (1989).
3. K. W. DeLong, K. B. Rochford, and G. I. Stegeman, "Effect of two-photon absorption on all-optical guided-wave devices," Appl. Phys. Lett. **55**(18), 1823–1825 (1989).
4. C. Koos, P. Vorreau, T. Vallaitis, P. Dumon, W. Bogaerts, R. Baets, B. Esembeson, I. Biaggio, T. Michinobu, F. Diederich, W. Freude, and J. Leuthold, "All-optical high-speed signal processing with silicon-organic hybrid slot waveguides," Nat. Photonics **3**(4), 216–219 (2009).
5. C. Koos, L. Jacome, C. Poulton, J. Leuthold, and W. Freude, "Nonlinear silicon-on-insulator waveguides for all-optical signal processing," Opt. Express **15**(10), 5976–5990 (2007).
6. M. Dinu, F. Quochi, and H. Garcia, "Third-order nonlinearities in silicon at telecom wavelengths," Appl. Phys. Lett. **82**(18), 2954–2956 (2003).
7. Q. Lin, J. Zhang, G. Piredda, R. W. Boyd, P. M. Fauchet, and G. P. Agrawal, "Dispersion of silicon nonlinearities in the near infrared region," Appl. Phys. Lett. **91**(2), 021111 (2007).
8. M. Hochberg, T. Baehr-Jones, G. Wang, M. Shearn, K. Harvard, J. Luo, B. Chen, Z. Shi, R. Lawson, P. Sullivan, A. K. Y. Jen, L. Dalton, and A. Scherer, "Terahertz all-optical modulation in a silicon-polymer hybrid system," Nat. Mater. **5**(9), 703–709 (2006).
9. H. K. Tsang, and Y. Liu, "Nonlinear optical properties of silicon waveguides," Semicond. Sci. Technol. **23**(6), 064007 (2008).
10. W. Bogaerts, R. Baets, P. Dumon, V. Wiaux, S. Beckx, D. Taillaert, B. Luyssaert, J. Van Campenhout, P. Bienstman, and D. Van Thourhout, "Nanophotonic waveguides in silicon-on-insulator fabricated with CMOS technology," J. Lightwave Technol. **23**(1), 401–412 (2005).
11. ePIXfab, http://www.epixfab.eu.
12. T. Michinobu, J. C. May, J. H. Lim, C. Boudon, J.-P. Gisselbrecht, P. Seiler, M. Gross, I. Biaggio, and F. Diederich, "A new class of organic donor-acceptor molecules with large third-order optical nonlinearities," in Chem. Commun.(2005), pp. 737–739.
13. B. Esembeson, M. L. Scimeca, T. Michinobu, F. Diederich, and I. Biaggio, "A high optical quality supramolecular assembly for third- order integrated nonlinear optics," Adv. Mater. **20**(23), 4584–4587 (2008).
14. T.-T. Kung, C.-T. Chang, J.-C. Dung, and S. Chi, "Four-Wave Mixing Between Pump and Signal in a Distributed Raman Amplifier," J. Lightwave Technol. **21**(5), 1164–1170 (2003).
15. M. Wu, and W. I. Way, "Fiber Nonlinearity Limitations in Ultra-Dense WDM Systems," J. Lightwave Technol. **22**(6), 1483–1498 (2004).

16. T. Vallaitis, C. Heine, R. Bonk, W. Freude, J. Leuthold, C. Koos, B. Esembeson, I. Biaggio, T. Michinobu, F. Diederich, P. Dumon, and R. Baets, "All-optical wavelength conversion at 42.7 Gbit/s in a 4 mm long silicon-organic hybrid waveguide," in Proc. Optical Fiber Communication Conference (OFC'09), San Diego (CA), USA, 22.–26.03.2009(2009), p. OWS3.
17. J. Mørk, and A. Mecozzi, "Theory of the ultrafast optical response of active semiconductor waveguides," J. Opt. Soc. Am. B **13**(8), 1803–1816 (1996).
18. T. Vallaitis, C. Koos, R. Bonk, W. Freude, M. Laemmlin, C. Meuer, D. Bimberg, and J. Leuthold, "Slow and fast dynamics of gain and phase in a quantum dot semiconductor optical amplifier," Opt. Express **16**(1), 170–178 (2008).
19. G. W. Rieger, K. S. Virk, and J. F. Young, "Nonlinear propagation of ultrafast 1.5 µm pulses in high-index-contrast silicon-on-insulator waveguides," Appl. Phys. Lett. **84**(6), 900–902 (2004).
20. M. A. Foster, A. C. Turner, R. Salem, M. Lipson, and A. L. Gaeta, "Broad-band continuous-wave parametric wavelength conversion in silicon nanowaveguides," Opt. Express **15**(20), 12949–12958 (2007).
21. B. L. Lawrence, M. Cha, J. U. Kang, W. Toruellas, G. Stegeman, G. Baker, J. Meth, and S. Etemad, "Large purely refractive nonlinear index of single crystal P-toluene sulphonate (PTS) at 1600 nm," Electron. Lett. **30**(5), 447–448 (1994).

1. Introduction

Highly nonlinear waveguides are key to on-chip integration of all-optical signal processing. All-optical signal processing devices should most preferably be implemented in widely available and cheap silicon technology and rely on the optical Kerr effect, hence enabling operation at THz bandwidth. However, while the Kerr effect in silicon is fast, its implementation is limited to low-power operation [1] to avoid impairments by the lifetime of free carriers generated by two-photon absorption (TPA) [2,3]. An alternative to the all-silicon technology is the silicon-organic hybrid (SOH) approach, which combines the highly developed silicon technology with a choice of organic cladding materials. The SOH approach allows the fabrication of ultra-dense highly field-confining silicon waveguides that combine record-high third-order nonlinear effects with low nonlinear losses [4].

The performance of highly nonlinear $\chi^{(3)}$ waveguides may be determined by four key parameters: the real and the imaginary part of the nonlinearity parameter γ, the chromatic dispersion D_2, and the linear waveguide loss α_0. At best, $\mathrm{Re}\{\gamma\}$ should be as large as possible, which requires a material with the largest possible nonlinear refractive index n_2 and the highest possible confinement to the effective area $A_{\mathrm{eff}}^{(3)}$,

$$\mathrm{Re}\{\gamma\} = \frac{n_2 \omega}{c A_{\mathrm{eff}}^{(3)}}, \qquad (1)$$

where ω is the angular frequency and c is the speed of light.

If the nonlinear loss due to two-photon absorption is significant, the peak power that can be used for cross and self-phase modulation is reduced. This places a fundamental limit on the achievable nonlinear effect at high power levels [2]. In that case, γ becomes complex: The real part of γ corresponds to the nonlinear refractive index change, and the imaginary part represents the nonlinear loss. The relative magnitude is described by the characteristic two-photon absorption figure of merit,

$$\mathrm{FOM}_{\mathrm{TPA}} = -\frac{1}{4\pi} \frac{\mathrm{Re}\{\gamma\}}{\mathrm{Im}\{\gamma\}}. \qquad (2)$$

Please note that in this definition $\mathrm{FOM}_{\mathrm{TPA}}$ represents a property of the waveguide. The figure of merit can also be defined to be a material property, relating the nonlinear index n_2 to the nonlinear TPA-coefficient α_2, $\mathrm{FOM}_{\mathrm{TPA}} = n_2/(\lambda \alpha_2)$. Both definitions are equivalent if n_2 and α_2 are uniform over the waveguide's cross section. In order to be able to achieve a

self-phase modulation (SPM)-induced phase shift $\Delta\phi_{NL} > \pi$, and to allow all-optical switching, waveguides need to exceed a value of $\text{FOM}_{\text{TPA}} > 0.5$ [2,3].

In this paper we compare the nonlinearity parameter γ, the chromatic dispersion D_2, the linear waveguide loss α_0, and the figure of merit of a conventional silicon wire waveguide with two different silicon-organic hybrid waveguides. It is found that silicon wire waveguides have a high nonlinearity parameter of up to $300\,000/(\text{W km})$, but are limited by the silicon figure of merit $\text{FOM}_{\text{TPA}} = 0.38 \pm 0.17$. In silicon waveguides two-photon absorption creates a large number of free carriers, which in turn lead to a slow dynamic due to the plasma effect. However, the combination of silicon waveguides with highly nonlinear organic cladding materials outperforms the simple silicon wire waveguide with respect to the two-photon absorption figure of merit with values up to $\text{FOM}_{\text{TPA}} = 2.19 \pm 0.25$ while retaining a high nonlinearity parameter $\gamma > 100\,000/(\text{W km})$. In this investigation we choose a nonlinear cladding material with a refractive index of $n = 1.8$ and a nonlinear refractive index of $n_2 = (1.7 \pm 0.8) \times 10^{-17}\ \text{m}^2/\text{W}$. The experiments were performed at 1550 nm.
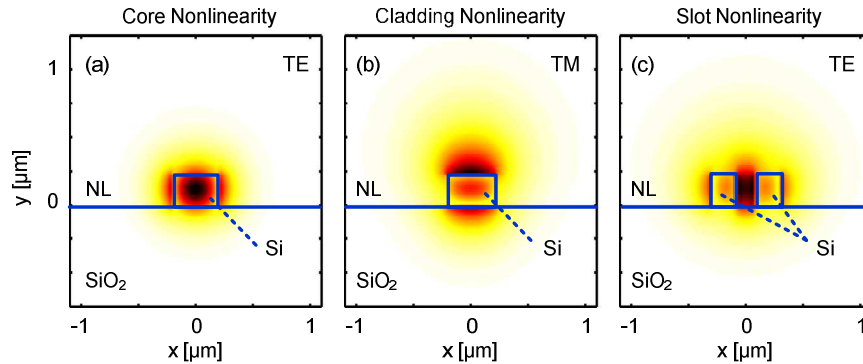
2. Waveguide structures

Fig. 1. Geometry and electric field distribution of three highly nonlinear CMOS-compatible waveguides. All silicon-on insulator waveguide structures are covered with an organic nonlinear cladding material (NL). (a) "*Core nonlinearity*": A strip waveguide operated in TE mode (dominant electric field component along the *x*-direction), where the light is concentrated in the waveguide core. The third-order nonlinearity is dominated by the complex-valued $\chi^{(3)}$ of silicon, while the effect of the cladding material is negligible. (b) "*Cladding nonlinearity*": A strip waveguide operated in TM mode (dominant electric field component along the *y*-direction). The optical signal is squeezed into the cladding allowing to exploit the real valued nonlinearity of the cladding. (c) "*Slot nonlinearity*": In the slot geometry, the light is almost completely confined to the slot filled with nonlinear material. For a cladding material with a real susceptibility, the TPA figure of merit is high for (b) and (c). All waveguides have been fabricated on the same chip with the same cladding material to allow for a fair comparison.

We consider here three generic nonlinear waveguide structures that exploit the nonlinearities of the core and the cladding material to a different extent [5]. Figure 1 shows the three proposed basic designs [5] along with the mode fields calculated for a cladding with $n = 1.8$. All structures are highly nonlinear but show characteristic differences in nonlinearity, dispersion, and the TPA figure of merit. They can be classified according to their real and imaginary part of the dominant nonlinearity.

2.1 Core nonlinearity

The strip waveguide operated in TE mode (dominant electric field component along the *x*-direction) is shown in Fig. 1(a). It consists of a single silicon strip waveguide. The field is

concentrated in the waveguide core ("core nonlinearity") and the nonlinear effect is maximized by the strong field confinement and dominated by the complex-valued $\chi^{(3)}$ of silicon. Hence, the figure of merit has a low value of $\text{FOM}_{\text{TPA}} \approx 0.35$ [6,7]. This structure is simple to fabricate, although care needs to be taken to reduce the sidewall roughness.

2.2 Cladding nonlinearity

The strip waveguide operated in TM mode (dominant electric field component along the *y*-direction) is shown in Fig. 1(b). It consists of a single silicon strip waveguide with a nonlinear cladding material. The mode is mostly guided in the cladding ("cladding nonlinearity"). The discontinuity of the refractive index at the waveguide top gives rise to a strong field enhancement in the cladding [8]. If the two-photon absorption in the organic cladding material is negligible, the waveguide figure of merit will be greatly improved. The top surface of the silicon strip is protected in all fabrication steps, so it remains flat and the propagation loss is low.

2.3 Slot nonlinearity

A different approach uses two narrow silicon strips separated by a small slot. Again, the whole structure is covered by a nonlinear organic cladding material. The mode distribution of a slot waveguide operated in TE mode is shown in Fig. 1(c). The light is strongly confined to the slot ("slot nonlinearity") due to the field enhancement at the silicon-organic interface. Because the intensity in the silicon strips is low, two-photon absorption will be lowest in the slot geometry, which leads to a greatly improved figure of merit. The propagation loss is higher than for the strip waveguides as the structure has four sidewalls that suffer from surface roughness. Further technological improvements might solve this problem.

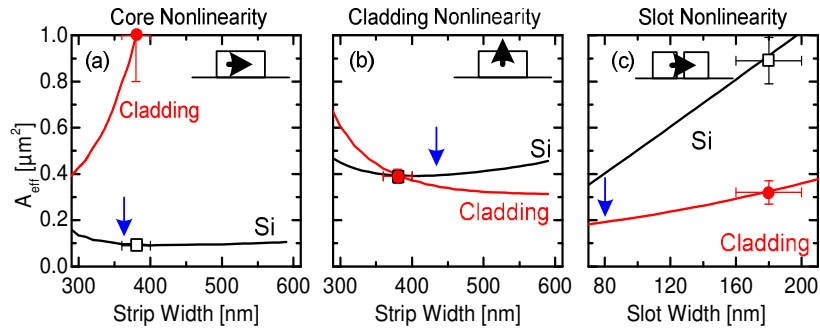## 2.4 Maximizing the nonlinearity coefficient of the three structures

Fig. 2. Effective areas for third order interaction in silicon (-, Si) and in the nonlinear cladding material (-, Cladding). For a fixed waveguide height of 220 nm the width of the strip or slot is varied. Following (1) the nonlinearity parameter is large for small effective areas. Small arrows (↓) mark the optimum dimensions [5]. The data points (,●) indicate the effective areas of the samples investigated in this paper. (a) In the waveguide with the core nonlinearity the dominant nonlinear contribution comes from the silicon, as the silicon effective area can be strongly minimized. (b) In waveguides with *cladding nonlinearity* both silicon and the nonlinear cladding material contribute alike. (c) The nonlinear effect of waveguides with *slot nonlinearity* mainly depends on the slot width. Decreasing the slot width decreases the effective area and thereby increases the nonlinearity parameter.

The nonlinearity coefficient can be maximized by the proper selection of the nonlinear material and by optimizing the geometry of the structure in order to minimize the effective areas of the mode fields depicted in Fig. 1. In this investigation we have contributions to the nonlinearity coefficient from the silicon ($n_2 = (4.5 \pm 1.5) \times 10^{-18} \, \text{m}^2/\text{W}$ [9]) and from the nonlinear organic cladding ($n_2 = (1.7 \pm 0.8) \times 10^{-17} \, \text{m}^2/\text{W}$). Figure 2 shows effective areas for

the third order interaction in silicon (-, Si) and the nonlinear cladding material (-, Cladding). For a fixed waveguide height of 220 nm the width of the strip or slot is varied. Small arrows mark technologically feasible dimensions that would optimize the nonlinearity parameter [5]. The data points (,●) indicate the effective areas of the samples investigated in this paper.

Figure 2(a) shows that the nonlinearity of waveguides with *core nonlinearity* is dominated by the silicon effective area. For waveguides with *cladding nonlinearity* in Fig. 2(b) both silicon and the nonlinear cladding material contribute alike. The nonlinear effect of waveguides with *slot nonlinearity* in Fig. 2(c) mainly depends on the slot width. Decreasing the slot width decreases the effective area and thereby increases the nonlinearity parameter. For a waveguide with a slot with of 80 nm, a two-fold increase of the nonlinearity parameter over the values measured here is possible.

3. Sample fabrication

The highly nonlinear silicon-organic hybrid slot waveguides [4] are based on silicon-on-insulator technology using the 193 nm DUV lithography [10] offered by ePIXfab [11]. Silicon strip waveguides with widths between 320 nm and 400 nm are fabricated from a 220 nm thick crystalline silicon layer on a 2 µm buried oxide buffer. Slot waveguides with slot widths between 160 nm and 200 nm are formed by two 220 nm wide silicon ribs.

The waveguides are filled and covered with molecular beam deposited DDMEBT (2-[4-(dimethylamino)phenyl]-3-{[4-(dimethylamino)phenyl]ethynyl}buta-1,3-diene-1,1,4,4-tetracarbonitrile) molecules). The nonlinear organic cladding obtained in such a way is highly homogeneous and has a refractive index of $n = 1.8$ with a nonlinear refractive index of $n_2 = (1.7 \pm 0.8) \times 10^{-17}\ \mathrm{m^2/W}$ [12,13]. Waveguide facets are as cleaved and no anti-reflection coating is applied, leading to a coupling loss to the strip and slot waveguides of (7…9) dB/facet and (4…6) dB/facet, respectively. The devices are 6.9 mm long and are operated without any temperature control.

4. Comparison of structures

In order to experimentally evaluate the properties of silicon-organic hybrid waveguide designs, we have fabricated waveguides of all basic types on the same chip. Four-wave mixing is used to measure the nonlinearity parameter, propagation losses and the dispersion of the waveguides. Heterodyne pump-probe measurements are used to measure the amplitude and phase dynamics and to calculate the two-photon absorption figure of merit. To reduce measurement errors, we average the data of multiple waveguides having slight variations in waveguide dimensions.

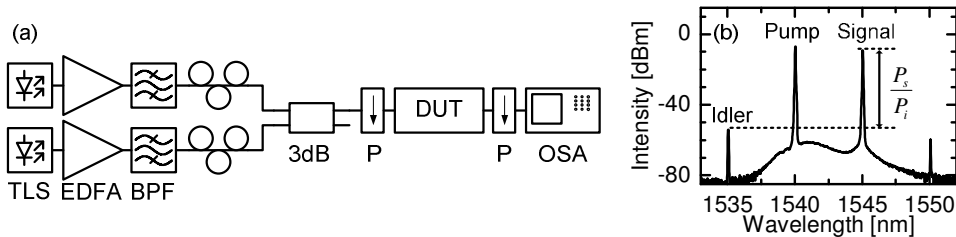*4.1 Nonlinearity parameter, dispersion and propagation loss*

Fig. 3. (a) Four-wave mixing setup and (b) example spectrum measured in a bandwidth of 0.1 nm. Co-polarized light from two amplified laser sources is launched into the device under test (DUT) and the four-wave mixing spectrum is recorded in an optical spectrum analyzer (OSA). From the ratio of the idler to the signal the nonlinearity parameter γ can be extracted. (TLS: tunable laser source, EDFA: erbium-doped fiber amplifier, BPF: optical band pass filter, P: polarizer)

The nonlinearity parameter, the dispersion and the propagation loss of the respective structures can be derived from four-wave mixing experiments.

The four-wave mixing setup is shown in Fig. 3(a). Co-polarized light from two amplified laser sources is launched into the device under test (DUT) using polarization-maintaining lensed fibers. The four-wave mixing spectrum is recorded in an optical spectrum analyzer (OSA). Polarization controllers and polarizers (P) are used to strictly separate between TE and TM polarization. The example spectrum in Fig. 3(b) shows the pump and signal waves, as well as the up and down-converted four-wave mixing products.
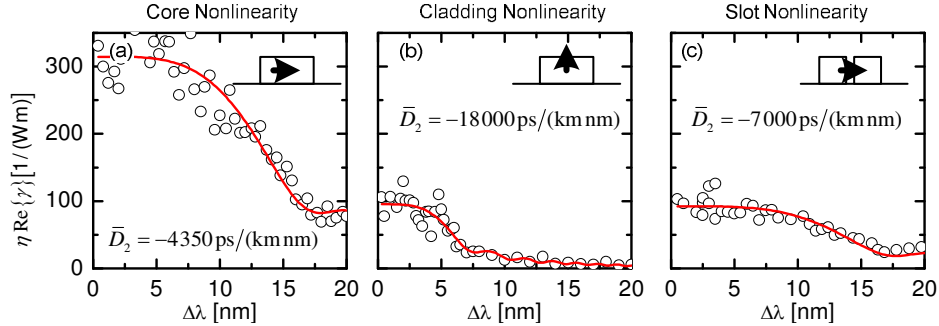

Fig. 4. Dependence of the nonlinearity parameter $\mathrm{Re}\{\gamma\}$ times η, the normalized four-wave mixing efficiency, as a function of the wavelength detuning $\Delta\lambda$; measurement (°) and fit (-). η describes the normalized degradation of the four-wave mixing efficiency with increasing phase mismatch, for perfect phase-matching $\eta = 1$ holds. The data are obtained by dividing the measured four-wave mixing conversion efficiency by the effective waveguide length, in order to emphasize the fundamental influence of dispersion, leaving out the technical issue of the propagation loss. The given parameters are averaged over multiple waveguides and measurements. All waveguides show high nonlinearities. (a) The strip waveguides with pure silicon core nonlinearity show the largest effect. (b) Waveguides with cladding nonlinearity have low linear losses but significant waveguide dispersion, which causes a large phase mismatch for detuning larger than 5 nm. (c) The slot waveguides show a strong nonlinear effect as well but provide larger phase-matching tolerance. All experimental results are summarized in Table 1.

Figure 4 shows the dependence of the nonlinearity parameter $\mathrm{Re}\{\gamma\}$ times the normalized four-wave mixing efficiency η on the wavelength detuning $\Delta\lambda$ for a 400 nm wide strip waveguide operated in TE and TM, and for a slot waveguide with a 160 nm slot. The quantity η describes the normalized degradation of the four-wave mixing efficiency with increasing phase mismatch, without mismatch $\eta = 1$ holds. The data are obtained by dividing the measured four-wave mixing conversion efficiency by the effective waveguide length (4), in order to emphasize the fundamental influence of dispersion, leaving out the technical issue of propagation loss.

The parameters extracted from the measurements are averaged over independent measurements of six waveguides for each design. Using a least squares fit procedure, the measurement of the idler power as a function of the frequency detuning between pump and signal allows to determine the nonlinearity parameter $\mathrm{Re}\{\gamma\}$, the linear propagation loss α_0 and the dispersion factor D_2.

Two photons of a strong pump are transformed into one photon of the signal wave and a new photon at the converted frequency $f_i = 2f_p - f_s$. For the characterization we used sufficiently low power levels (< 15 dBm on-chip power), such that nonlinear losses due to two-photon absorption were negligible. For a given launch power $P_p(0)$ of the pump and of the signal $P_s(0)$, the power $P_i(z)$ of the idler wave after a propagation length L becomes

$$P_i(L) = e^{-\alpha_0 L} \left(\eta \operatorname{Re}\{\gamma\} P_p(0) L_{\text{eff}} \right)^2 P_s(0), \tag{3}$$

where η is the four-wave mixing efficiency and L_{eff} is the effective waveguide length

$$L_{\text{eff}} = \frac{1 - e^{-\alpha_0 L}}{\alpha_0}. \tag{4}$$

For a center wavelength λ_p in a waveguide with the dispersion factor D_2, the total phase mismatch for a detuning $\Delta\lambda = \lambda_p - \lambda_s$ is

$$\Delta\beta = \frac{2\pi\lambda^2 D_2}{c} \Delta f_{ik} \Delta f_{jk} = \frac{2\pi c D_2}{\lambda_p^2} (\Delta\lambda)^2, \tag{5}$$

and the four-wave mixing efficiency for this phase mismatch is then given by [14,15]

$$\eta^2 = \frac{\alpha_0^2}{\alpha_0^2 + \Delta\beta^2} \left[1 + 4e^{-\alpha_0 L} \frac{\sin^2(L\Delta\beta/2)}{\left(1 - e^{-\alpha_0 L}\right)^2} \right]. \tag{6}$$

In our measurements, waveguides with pure silicon *core nonlinearity* and dimensions close to the theoretical optimum [5] show the largest nonlinear effect. For waveguide widths of $(360\ldots400)\,\text{nm}$ an averaged nonlinearity parameter of $\bar{\gamma} = (307\,000 \pm 17\,000)/(\text{W km})$ is found, close to the theoretical maximum of $\gamma_{\max} \approx 350\,000/(\text{W km})$. Dispersion and propagation loss are measured to be $\bar{D}_2 = (-4350 \pm 150)\,\text{ps}/(\text{km nm})$ and $\bar{\alpha}_0 = (1.1 \pm 0.1)\,\text{dB/mm}$, respectively.

Strip waveguides with *cladding nonlinearity* show a large averaged nonlinearity parameter of $\bar{\gamma} = (108\,000 \pm 17\,000)/(\text{W km})$ for $(360\ldots400)\,\text{nm}$ wide strips. A propagation loss of $\bar{\alpha}_0 = (1.0 \pm 0.1)\,\text{dB/mm}$ is found. This value is higher than expected for a device with very low interface roughness. But because the mode extends deeply into the cladding, scattering at the sample surface gives rise to additional propagation loss. The significant waveguide dispersion of $\bar{D}_2 = (-18\,000 \pm 2\,300)\,\text{ps}/(\text{km nm})$ causes a large phase mismatch for a detuning larger than 5 nm, see Fig. 4(b).

Waveguides with *slot nonlinearity* also show a strong nonlinearity parameter of $\bar{\gamma} = (100\,000 \pm 13\,000)/(\text{W km})$. This is remarkable because the waveguide height of $220\,\text{nm}$ and the slot width of $(160\ldots200)\,\text{nm}$ are far from the optimum that is reached for much smaller slot widths—see Fig. 2(c)—which could allow nonlinearity parameters beyond $10^6/(\text{W km})$ [5]. The total nonlinear effect is limited by a low effective waveguide length of $L_{\text{eff}} = 2.6\,\text{mm}$, due to an increased linear loss of $\bar{\alpha}_0 = (1.5 \pm 0.1)\,\text{dB/mm}$. The dispersion of $\bar{D}_2 = (-7\,000 \pm 400)\,\text{ps}/(\text{km nm})$ although large, is still sufficiently low to enable all-optical wavelength conversion at 42.7 Gbit/s [16] and demultiplexing at 170.8 Gbit/s [4] in a 4 mm long slot waveguide. All experimental results are summarized in Table 1.

Table 1. Dimensions and optical properties of basic silicon-organic hybrid waveguide designs determined from four-wave mixing and heterodyne pump-probe experiments at a center wavelength of λ = 1.55 µm.
(*) Effective areas of silicon and nonlinear cladding material are obtained from a finite-element simulation.

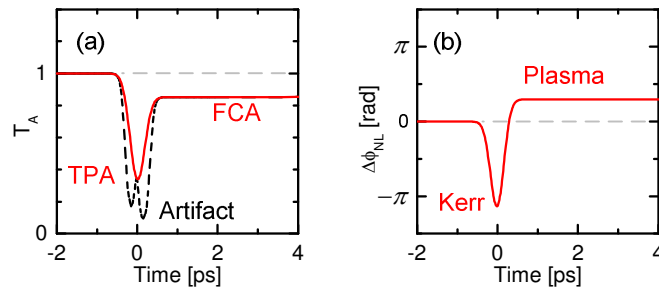| Design	Core	Cladding	Slot
$\mathrm{Re}\{\gamma\}$ [1/(W km)]	307 000 ± 17 000	108 000 ± 17 000	100 000 ± 13 000
$\mathrm{FOM_{TPA}}$	0.38 ± 0.17	1.21 ± 0.19	2.19 ± 0.25
D_2 [ps/(km nm)]	−4350 ± 150	−18000 ± 2300	−7000 ± 400
α_0 [dB/mm]	1.1 ± 0.1	1.0 ± 0.1	1.5 ± 0.1
a_{cp} [dB/facet]	8.8 ± 0.2	7.5 ± 0.2	5.0 ± 1.0
Height [nm]	220	220	220
Rib Width [nm]	360…400	360…400	220
Slot Width [nm]	0	0	160…200
$A_{\mathrm{eff},Si}^{(3)}$ [µm^2]	0.09*	0.39*	0.89*
$A_{\mathrm{eff},NL}^{(3)}$ [µm^2]	1.25*	0.39*	0.29*

4.2 Figure of merit measurement

Fig. 5. Schematic illustration of (a) amplitude and (b) phase effects. At zero time delay, the Kerr effect causes an instantaneous phase change. If free carriers are created by two-photon absorption of the pulse, the plasma effect leads to an undesired phase change with the opposite sign and a long time constant. The amplitude transmission (a) shows the instantaneous loss caused by two-photon absorption and a permanently reduced transmission due to free carrier absorption. The dashed line shows the spectral artifact of the measurement principle, which is expected for strong Kerr media [17].

To characterize the nonlinear dynamics, heterodyne pump-probe measurements were performed. Simultaneous measurements of amplitude and phase dynamics allow to determine the two-photon absorption figure of merit (2) with high precision and without any free parameters like the effective area $A_{\mathrm{eff}}^{(3)}$. In order to resolve amplitude and phase dynamics of the proposed waveguide designs, we have used a heterodyne pump-probe technique [18].

In the pump-probe setup a strong pump pulse induces nonlinearities in the waveguide, at a center wavelength of 1550 nm. A weak probe pulse launched after the pump pulse then experiences changes in the amplitude transmission and the refractive index of the waveguide. By superimposing the probe pulse with a local reference pulse in an unbalanced Michelson interferometer, a beating signal is created in a photodiode. A lock-in amplifier is then used to resolve the amplitude and phase information. By changing the time delay between pump and probe pulses, we are able to sample the device dynamics with sub-picoseconds resolution.

Figure 5 shows a schematic illustration of the effects found in the (a) amplitude and (b) phase dynamics of nonlinear silicon waveguides. At zero time delay, the Kerr effect causes an

instantaneous phase change. For the time dependency of $\exp(j\omega t)$ used in this paper, the change of the refractive index caused by the Kerr effect is positive and given by $\Delta n = -\phi_{NL}\lambda/(2\pi L_{eff})$. If free carriers are created by two-photon absorption, the plasma effect leads to an undesired phase change with the opposite sign and a long time constant. The amplitude transmission Fig. 5(a) shows the instantaneous loss caused by two-photon absorption, and a permanently reduced transmission due to free carrier absorption.

The dashed line depicts an artifact of the measurement technique. In strong Kerr media the nearly instantaneous phase shift causes a very strong frequency shift $\Delta f = d\phi_{NL}/dt$ of the probe pulse for non-zero time delay. This violates the assumption that the frequency difference between probe and reference pulses is fixed. A lock-in amplifier tuned to this difference frequency is unable to correctly detect the signal. Hence, the measured transmission seems to drop to nearly zero. As this drop is only caused by a violation of the measurement assumptions, it is treated as an artifact [17].

Figure 6 shows amplitude transmission T_A and phase $\Delta\phi_{NL}$ dynamics of the three highly nonlinear waveguides. All waveguides show strong Kerr nonlinearities, the main difference is in the strength of the two-photon absorption and the amount of long lasting changes due to generated free carriers.
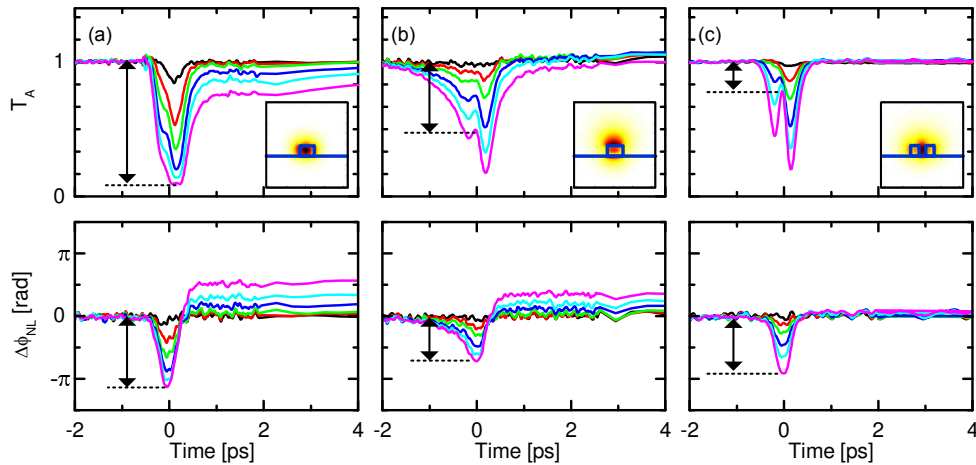

Fig. 6. Amplitude transmission T_A and phase $\Delta\phi_{NL}$ dynamics of the highly nonlinear waveguides for different pump power levels. All waveguides show strong Kerr nonlinearities. However, the (a) silicon *core nonlinearity* waveguide shows strong two-photon absorption accompanied with simultaneous strong free-carrier absorption. The experiment leads to a figure of merit $FOM_{TPA} = 0.38 \pm 0.17$. (b) The waveguide with *cladding nonlinearity* shows a significantly lower detrimental TPA effect. It has a $FOM_{TPA} = 1.21 \pm 0.19$. (c) Waveguide with *slot nonlinearity* showing a Kerr nonlinearity with nearly no two-photon absorption, negligible free carrier absorption, and a $FOM_{TPA} = 2.19 \pm 0.25$.

The strong pump signal with power P_P experiences linear losses α_0 and nonlinear losses α_2 due to two-photon absorption (TPA) and self-phase modulation (SPM) due to the Kerr effect. The change of the power $P_P(z)$ and phase $\phi_{P,NL}$ are given by [2]

$$\frac{dP_P(z)}{dz} = -\alpha_0 P_P(z) + 2\,\mathrm{Im}\{\gamma\}\,P_P^2(z), \tag{7}$$

$$\frac{d\phi_{P,NL}(z)}{dz} = \mathrm{Re}\{\gamma\} P_P(z), \tag{8}$$

where α_0 is the linear loss and λ is the center wavelength. Third-order nonlinearities are described by the nonlinear refractive index n_2 and the two-photon absorption coefficient α_2. The resulting pump power $P_P(z)$ for a launched pump power $P_{P,0}$ is

$$P_P(z) = \frac{e^{-\alpha_0 z}}{1 - 2L_{\mathrm{eff}}\, \mathrm{Im}\{\gamma\} P_{P,0}} P_{P,0}. \tag{9}$$

For zero time delay, pump and probe pulses occupy the same time slot. The weak probe pulse experiences negligible two-photon absorption, but considerable cross-two-photon absorption (XTPA) as well as cross-phase-modulation (XPM). The change of power $P_S(z)$ and phase $\phi_{NL}(z)$ are

$$\frac{dP_S(z)}{dz} = -\alpha_0 P_S(z) + 4\,\mathrm{Im}\{\gamma\} P_P(z) P_S(z), \tag{10}$$

$$\frac{d\phi_{NL}(z)}{dz} = 2\,\mathrm{Re}\{\gamma\} P_P(z). \tag{11}$$

Because of the known pump power (9), Eq. (10) can be integrated to yield

$$P_S(z) = \frac{e^{-\alpha_0 z}}{\left(1 - 2L_{\mathrm{eff}}\, \mathrm{Im}\{\gamma\} P_{P,0}\right)^2} P_{S,0}. \tag{12}$$

If for each time delay two measurements are taken, one with a pump of known power $P_{P,0}$ and one with a blocked beam $P_{P,0} = 0$, the power transmission T_P and the nonlinear phase change $\Delta\phi_{NL}$ become

$$T_P = \frac{P_S(P_P > 0)}{P_S(P_P = 0)} = \frac{1}{\left(1 - 2L_{\mathrm{eff}}\, \mathrm{Im}\{\gamma\} P_{P,0}\right)^2}, \tag{13}$$

$$\Delta\phi_{NL} = -\frac{\mathrm{Re}\{\gamma\}}{\mathrm{Im}\{\gamma\}} \ln\left(1 - 2L_{\mathrm{eff}}\, \mathrm{Im}\{\gamma\} P_{P,0}\right). \tag{14}$$

Amplitude transmission $T_A = T_P^{0.5}$ and nonlinear phase change $\Delta\phi_{NL}$ are quantities that can be directly measured using the heterodyne pump-probe technique. Without the need to calculate an effective area $A_{\mathrm{eff}}^{(3)}$, solving (13) and (14) with respect to $\mathrm{Re}\{\gamma\}/\mathrm{Im}\{\gamma\}$ yields an expression for the two-photon absorption figure of merit that only relies on these measured quantities, and is a characteristic property of the waveguide,

$$\mathrm{FOM}_{\mathrm{TPA}} = -\frac{1}{4\pi}\frac{\mathrm{Re}\{\gamma\}}{\mathrm{Im}\{\gamma\}} = -\frac{\Delta\phi_{NL}}{4\pi \ln T_A}. \tag{15}$$

Pump-probe measurements of the silicon *core nonlinearity* in Fig. 6(a) show strong two-photon absorption and strong free-carrier absorption at the same time. This leads to a figure of merit of $\mathrm{FOM}_{\mathrm{TPA}} = 0.38 \pm 0.17$, in good agreement with values found for unclad silicon waveguides [6,9]. As a side effect of the strong two-photon absorption, free carriers with a life time of 1.2 ns are generated, leading to free-carrier absorption and slow phase change due to the plasma effect. For high speed applications, free carriers will accumulate, thereby reducing the nonlinear effect and leading to patterning effects.

The waveguide with *cladding nonlinearity* is shown in Fig. 6(b). As only a minor fraction of the intensity is still guided in the silicon, the detrimental effects are already reduced and the figure of merit is improved to $\text{FOM}_{\text{TPA}} = 1.21 \pm 0.19$. At high peak power, smaller numbers of free carriers are generated, leading to a reduced plasma effect. The two lobes visible in the transmission dynamics are the spectral artifact due to the rapid phase change, as explained in Fig. 5.

Waveguides with *slot nonlinearity* in Fig. 6(c) show a strong Kerr nonlinearity with nearly no two-photon absorption and negligible free carrier absorption. The two-photon absorption figure of merit is $\text{FOM}_{\text{TPA}} = 2.19 \pm 0.25$, which enables all-optical signal processing at highest bit rates [4]. Though, while the nonlinearity parameter of the silicon strip waveguide with core nonlinearity is higher, the nonlinearity of the slot geometry shows much smaller nonlinear losses and thus a much better scalability with peak power.

If the effective area of a nonlinear waveguide is known, the pump-probe traces also allow to determine the two-photon absorption parameter α_2. For a simple silicon strip waveguide the intensity is known, as the effective area $A_{\text{eff,Si}}^{(3)}$ can be easily derived numerically. For a peak pulse power P_{P0}, the inverse power transmission of the strong pump pulse depends linearly on the on-chip intensity $I_{P,0} = P_{P,0} / A_{\text{eff,Si}}^{(3)}$,

$$\frac{1}{T_P} = \frac{1}{T_A^2} = 1 - 2\,\text{Im}\{\gamma\}\,P_{P,0}\,L_{\text{eff}}. \tag{16}$$
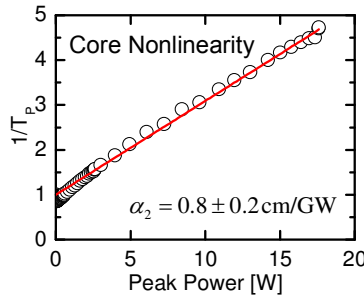

Fig. 7. Measured inverse power transmission $1/T_P$ of a silicon strip waveguide with core nonlinearity as a function of the on-chip peak power. For an effective waveguide length of $L_{\text{eff}} = 2.5\,\text{mm}$, the two-photon absorption coefficient is calculated from the slope of a linear fit to a value of $\alpha_2 = (0.8 \pm 0.2)\,\text{cm/GW}$.

Figure 7 shows the inverse power transmission for a 390 nm wide silicon strip waveguide. By using the measured dispersion of $D_2 = -4400\,\text{ps/(km\,nm)}$ (see Table 1) to calculate the average peak power, an effective area of $0.092\,\mu\text{m}^2$, and an effective length of $L_{\text{eff}} = 2.5\,\text{mm}$, the imaginary part of γ due to two-photon absorption is calculated from the slope of a linear fit to a value of $\text{Im}\{\gamma\} = -41.6/(\text{W\,m})$. Since all the TPA originates form the silicon core, and since the effective area within the core is known, we can derive the TPA-coefficient of silicon, $\alpha_2 = 0.8\,\text{cm/GW}$. This is in good agreement with previous work [6,19]. As the pulse width in the waveguide can only be estimated with an uncertainty of 20%, the total error for α_2 is $\pm 0.2\,\text{cm/GW}$. However, for the calculation of the figure of merit in (15), these and other inaccuracies (e. g., for $A_{\text{eff}}^{(3)}$) cancel.

5. Conclusions

Highly nonlinear silicon waveguides with core, cladding and slot nonlinearity have been fabricated. Key parameters have been analyzed and are summarized in Table 1. As each design shows characteristic advantages, the optimum design strongly depends on the intended application.

For applications at repetition rates below 1 GHz or if signal distortion due to free carrier effects can be tolerated, pure silicon strip waveguides with *core nonlinearity* are the easiest solution. By confining the light to small waveguide cross-sections, very high nonlinearity parameters can be reached, up to a record value measured in silicon of $\gamma = (307\,000 \pm 17\,000)/(\text{W km})$. However, this high value of the nonlinearity parameter is resonantly enhanced, and the fundamental two-photon absorption limitation for switching applications cannot be overcome. The waveguides are easy to fabricate and show low dispersion. By engineering the waveguide dimensions to optimize the zero dispersion wavelength, highly efficient wavelength conversion is possible [20].

For applications that simultaneously require good conversion efficiency, a high figure of merit and multi-wavelength operation, waveguides with *cladding nonlinearity* are the optimum design. Strip waveguides are easy to fabricate and easy to cover with nonlinear cladding materials. The figure of merit with a value of $\text{FOM}_{\text{TPA}} = 1.21 \pm 0.19$ is sufficient for all-optical switching. Because the electric field in TM mode is oriented perpendicularly to the wafer surface, even cladding materials which have very high nonlinear refractive indices but are difficult to deposit could be used, possibly increasing the nonlinearity parameter by a factor of 10 [21]. The significant waveguide dispersion can be even used to limit the nonlinear interaction to a detuning of 5 nm, enabling multi-wavelength operation.

For high speed applications, waveguides with *slot nonlinearity* will provide the best signal quality. The light is strongly confined to the slot, so two-photon absorption and associated free carrier effects in silicon can be avoided. Silicon-organic hybrid slot waveguides are highly nonlinear showing potential for nonlinearity parameters beyond $10^6/(\text{W km})$. In addition, they exhibit the best figure of merit of $\text{FOM}_{\text{TPA}} = 2.19 \pm 0.25$ reported for CMOS-compatible waveguides. As this allows the use of high peak powers, the waveguide length can be kept small, and phase mismatch due to dispersion is negligible, thus enabling all-optical signal processing at highest bit rates [4]. Future improvements in the fabrication process will reduce the limiting propagation loss and allow to move to even smaller slot widths, significantly increasing the confinement to the slot. In combination with improved nonlinear cladding materials, this will enable all-optical switching in millimeter-long devices.

Acknowledgments